



Targeting oncogenic KRAS with molecular brush-conjugated antisense oligonucleotides

Dali Wang^{a,1}, Qiwei Wang^{b,c,1}, Yuyan Wang^{a,1}, Peiru Chen^a, Xueguang Lu^d, Fei Jia^a, Yehui Sun^a, Tingyu Sun^a, Lei Zhang^a, Fangyuan Che^a, Jialu He^a, Liming Lian^a, Gemma Morano^a 📵, Michael Shen^a, Mengqi Ren^a, Sijia S. Dong^a 📵, Jean J. Zhao^{b.c,2} 📵, and Ke Zhang^{a.e,f,2} 📵

Edited by Brent Sumerlin, University of Florida, Gainesville, FL; received July 20, 2021; accepted May 12, 2022 by Editorial Board Member Chad A. Mirkin

The mutant form of the guanosine triphosphatase (GTPase) KRAS is a key driver in human tumors but remains a challenging therapeutic target, making $KRAS^{MUT}$ cancers a highly unmet clinical need. Here, we report a class of bottlebrush polyethylene glycol (PEG)-conjugated antisense oligonucleotides (ASOs) for potent in vivo KRAS depletion. Owing to their highly branched architecture, these molecular nanoconstructs suppress nearly all side effects associated with DNA-protein interactions and substantially enhance the pharmacological properties of the ASO, such as plasma pharmacokinetics and tumor uptake. Systemic delivery to mice bearing human non-small-cell lung carcinoma xenografts results in a significant reduction in both KRAS levels and tumor growth, and the antitumor performance well exceeds that of current popular ASO paradigms, such as chemically modified oligonucleotides and PEGylation using linear or slightly branched PEG. Importantly, these conjugates relax the requirement on the ASO chemistry, allowing unmodified, natural phosphodiester ASOs to achieve efficacy comparable to that of chemically modified ones. Both the bottlebrush polymer and its ASO conjugates appear to be safe and well tolerated in mice. Together, these data indicate that the molecular brush-ASO conjugate is a promising therapeutic platform for the treatment of KRAS-driven human cancers and warrant further preclinical and clinical development.

NSCLC | KRAS | antisense oligonucleotide | molecular brush | gene regulation

Mutationally activated RAS genes (HRAS, KRAS, and NRAS) are the most frequently mutated proto-oncogenes in human cancer (27%), with KRAS being the most mutated oncogene (85% of all RAS missense mutations) (1). KRAS functions as a molecular switch cycling between guanosine triphosphate (GTP)-bound (on) and guanosine diphosphate (GDP)-bound (off) states to affect intracellular signaling through cell-surface receptors. The missense mutation of KRAS aberrantly activates the protein into a hyperexcitable state by attenuating its guanosine triphosphatase (GTPase) activity, which results in an accretion of GTP-bound, activated KRAS and persistent activation of downstream signaling pathways (2). Mutations of KRAS are associated with poor prognosis in several cancers, and a substantial body of evidence has confirmed the role of KRAS in the initiation and maintenance of cancer, thus making KRAS an important therapeutic target (3-6). KRAS has long been considered undruggable due to the lack of deep binding pockets. However, in 2013, it was shown that the cysteine residue of the G12C mutant give rise to a new pocket that can be selectively targeted by small-molecule binders (3, 7). This development led to the accelerated approval of sotorasib and shortly thereafter adagrasib, the first-in-class drug KRAS inhibitors for advanced non-small-cell lung carcinoma (NSCLC) (8). The breakthrough therapy designation of both compounds speaks to the significance of the target. Nonetheless, the G12C mutation only occurs in a small percentage of KRAS^{MUT} cancers—predominantly in lung adenocarcinomas and, at a lower frequency, in colorectal cancer and pancreatic ductal adenocarcinomas (44%, 11%, and 3%, respectively) (1, 9). Thus, RAS inhibition and the development of novel therapies remain an unmet clinical need.

The difficulty in developing small-molecule inhibitors for KRAS has heightened the importance of alternative methods targeting the oncogene, for example using antisense oligonucleotides (ASOs) (10), which offer a possibility to yield drugs for targets that have proven to be intractable to traditional drug modalities (11, 12). Nucleic acid drugs are attractive for traditionally undruggable targets due to their ability to selectively bind with human or pathogen transcriptome to knock down gene expression, to alter messenger RNA (mRNA) splicing, to target trinucleotide repeat disorders, to affect noncoding RNAs involved in transcriptional and epigenetic regulation, to up-regulate target genes, and to edit the genome (13). To date, 11 oligonucleotide drugs have been approved by the US Food and Drug Administration, four of which were approved in the past 3 y (14).

Despite these clinical advances, nucleic acid drugs are being mainly developed for rare diseases originating from the liver or in tissues that can be treated by local injection, such

Significance

We report a molecular brush-based oligonucleotide therapeutics platform which uniquely provides conjugated antisense oligonucleotides with binding selectivity, improved pharmacological properties, and an unusual biodistribution profile. These improvements lead to superior in vivo performance compared with the state of the art in *KRAS^{MUT}*-driven non-small-cell lung carcinoma mouse models with minimal side effects and may eventually broaden the disease areas where a nucleic acid-based treatment can be developed.

Author affiliations: aDepartment of Chemistry and Chemical Biology, Northeastern University, Boston, MA 02115; ^bDepartment of Cancer Biology, Dana-Farber Cancer Institute, Boston, MA 02115; ^cDepartment of Machanistry Machan Northeastern University, Boston, MA 02115

Author contributions: D.W. and K.Z. designed research; D.W., Q.W., Y.W., P.C., X.L., F.J., Y.S., T.S., L.Z., F.C., J.H., L.L., G.M., M.S., and M.R. performed research; S.S.D. carried out molecular dynamics simulation; D.W., Q.W., Y.W., J.J.Z., and K.Z. analyzed data; J.J.Z. contributed to in vivo study design and implementation; and D.W. and K.Z. wrote the paper.

The authors declare no competing interest.

This article is a PNAS Direct Submission. B.S. is a guest editor invited by the Editorial Board.

Copyright © 2022 the Author(s). Published by PNAS. This article is distributed under Creative Commons Attribution-NonCommercial-NoDerivatives License 4.0

¹D.W., Q.W., and Y.W. contributed equally to this work.

²To whom correspondence may be addressed. Email: jean_zhao@dfci.harvard.edu or k.zhang@northeastern.

This article contains supporting information online at http://www.pnas.org/lookup/suppl/doi:10.1073/pnas 2113180119/-/DCSupplemental.

Published July 14, 2022.

as the spinal cord or the eye (15). The limited use cases and overall slow bench-to-bedside translation reflect the intrinsic difficulties associated with oligonucleotide drugs (16). Unmodified, naked oligonucleotides are easily degraded by nucleases, can undergo rapid renal and hepatic clearance, and are hopelessly incapable of cellular uptake owing to a combination of hydrophilicity and high molecular weight (17). Advanced delivery systems (polycationic polymers, nanoparticles, liposomal formulations, etc.) have been developed to overcome these difficulties (18-20). However, other than liposomes, most carrier systems still need to be proven relevant in a clinical setting (15). Challenges include toxicity, immunogenicity, consistency in formulation, chemical and in vivo stability, release control, and problems associated with large-scale manufacturing (21-23). On the other hand, nucleic acid modification chemistries have been far more successful for clinical translation, with all currently approved oligonucleotide drugs adopting one or more forms of modifications (24, 25). For example, the phosphorothioates (PS) have greatly improved enzymatic stability, potency, and duration of oligonucleotides in vivo, making it possible to bypass the need for complex carriers (26). However, although nonspecific binding between PS and serum proteins improves tissue uptake and reduces renal clearance, the blood pharmacokinetics (PK) of PS drugs remains very poor (27, 28). The liver and the kidney are often the organs that receive most of the injected dose, followed by the bone marrow, adipocytes, and lymph nodes (29). To achieve a therapeutically relevant concentration at tumor tissues, the dosage would often exceed safety tolerance (24). In fact, PS show increased potential for nonspecific adverse effects including induction of stress responses, prolongation of activated partial thromboplastin time, thrombocytopenia, and increased serum transaminase activities (30, 31). Mipomersen, the first systemically administered PS drug that treats homozygous familial hypercholesterolemia, was only approved in the United States and not Europe due to concerns of adverse toxic effects (32). Therefore, a safe, simple, and efficient nucleic acid delivery system that can improve nuclease stability, address nonliver organs, and minimize off-target effects may prove to be the important missing link between oligonucleotides and their adoption for cancer treatment.

Recently, we have developed a form of PEGylated oligonucleotides, termed polymer-assisted compaction of DNA (pacDNA), which consists of a small number of ASOs (typically one to five) tethered to the backbone of a bottlebrush polyethylene glycol (PEG) via the 3', 5', or an internal position of the ASO (33, 34). The bottlebrush architecture of the pacDNA conceals the ASO within an intermediate-density PEG environment, which provides the ASO with sterics-based selectivity: Hybridization with a complementary strand is unaffected, but access by proteins, which are much larger in cross-section diameter, is significantly hindered (35). Such selectivity reduces enzymatic degradation and most unwanted side effects stemming from specific or nonspecific oligonucleotide-protein interactions (e.g., coagulopathy and unwanted immune system activation), while substantially improving the plasma PK and concentration in nonliver organs (36). Importantly, the observed physiochemical and biopharmaceutical enhancements over naked nucleic acids are realized using predominantly PEG, which is generally regarded as safe for therapeutic applications (37).

Herein, we explore the pacDNA in the context of treating NSCLC harboring $KRAS^{MUT}$. A library of pacDNA constructs having an identical ASO base sequence but with variation in ASO chemistry, releasability, and degree of steric shielding was tested. We report the in vitro and in vivo pharmacological properties

of these materials, describe the dosage-dependent antitumor response in mice bearing $KRAS^{MUT}$ NSCLC xenografts, and characterize the safety profile of the pacDNA in mice. Comparing an optimized pacDNA with a clinical ASO targeting the same transcript region (AZD4785), pacDNA achieved more pronounced tumor suppression levels than AZD4785 but at a fraction (2.5%) of the dosage and with reduced dosing frequency. In addition, the treatment was free of common deleterious side effects such as acute toxicity, inflammation, and immunogenic side effects. Overall, the pacDNA system we established here may offer a clinically viable approach to addressing KRAS-driven human cancers.

Results

Physicochemical Properties of pacDNA. The ASO sequence of choice is the same as that of AZD4785, a cEt-modified clinical compound targeting the 3' untranslated region of the KRAS mRNA (Fig. 1A) (11). Although the targeted region is away from mutation sites (thus, wild-type KRAS is also depleted), AZD4785 has shown selectivity toward $KRAS^{MUT}$ cells for inhibiting proliferation and is potent against several mutant isoforms. However, a Phase I clinical study of AZD4785 was unsuccessful due to insufficient target depletion (15, 38). Indeed, the oncological use of ASOs is challenged by their short plasma halflife and limited tumor-site accumulation, necessitating frequent injections which can cause undesirable peak-to-valley fluctuations of drug concentration, increased nonantisense side effects, reduced patient compliance, and increased cost (39). Adopting the same sequence as AZD4785 for pacDNA allows one to draw direct comparisons with an existing body of preclinical data.

Here, a library of PEGylated ASO structures have been designed to elucidate the in vivo importance of various structural parameters and to optimize ASO potency and pharmacological properties. These pacDNA structures vary in ASO composition (natural and chemically modified), conjugation site (sequence termini or internal position), and releasability (stable or bioreductively cleavable) (Fig. 1 B-D and SI Appendix, Table S1). Additionally, a Y-shaped PEG (40 kDa), which has been adopted in the oligonucleotide drug, pegaptanib (brand name Macugen) (40), is used to form an ASO conjugate as a polymer architecture control.

The brush polymer was prepared via sequential ring-opening metathesis polymerization (ROMP) of 7-oxanorbornenyl bromide (ON-Br) and norbornenyl PEG (N-PEG), to yield a diblock architecture (pONBr₅-b-pNPEG₃₀, polydispersity index <1.2). Following azide substitution and subsequent coupling with dibenzocyclooctyne (DBCO)-modified ASO strands via the strain-promoted copper-free click chemistry (41), pacDNA structures with an average of 2.0 ASO strands per polymer were prepared (~95% yield; *SI Appendix*, Figs. S1 and S2). The conjugates were purified by aqueous size-exclusion chromatography (SI Appendix, Fig. S3A) and lyophilized for storage. Agarose gel electrophoresis (AGE, 1%) indicates the successful synthesis of the pacDNA and the Y-shaped PEG-ASO conjugates, which are free of unconjugated ASO (SI Appendix, Fig. S3B). Note that the upward gel migration of the pacDNA is a consequence of the transient interaction of PEG with cations in the buffer, and not because of a net positive charge (42). Indeed, ζ potential measurements indicate that the pacDNAs have a slight negative charge (-1 to -3 mV) in Nanopure water, which is significantly below that of free DNA (\sim -35 mV) and the Y-shaped PEG-ASO conjugate (~-17 mV; SI Appendix, Fig. S3C). Being molecular nanoparticles, the pacDNAs exhibit a spherical morphology with a dry-state diameter of ~29 nm, as evidenced by transmission electron microscopy (SI Appendix, Fig. S3 D and E).

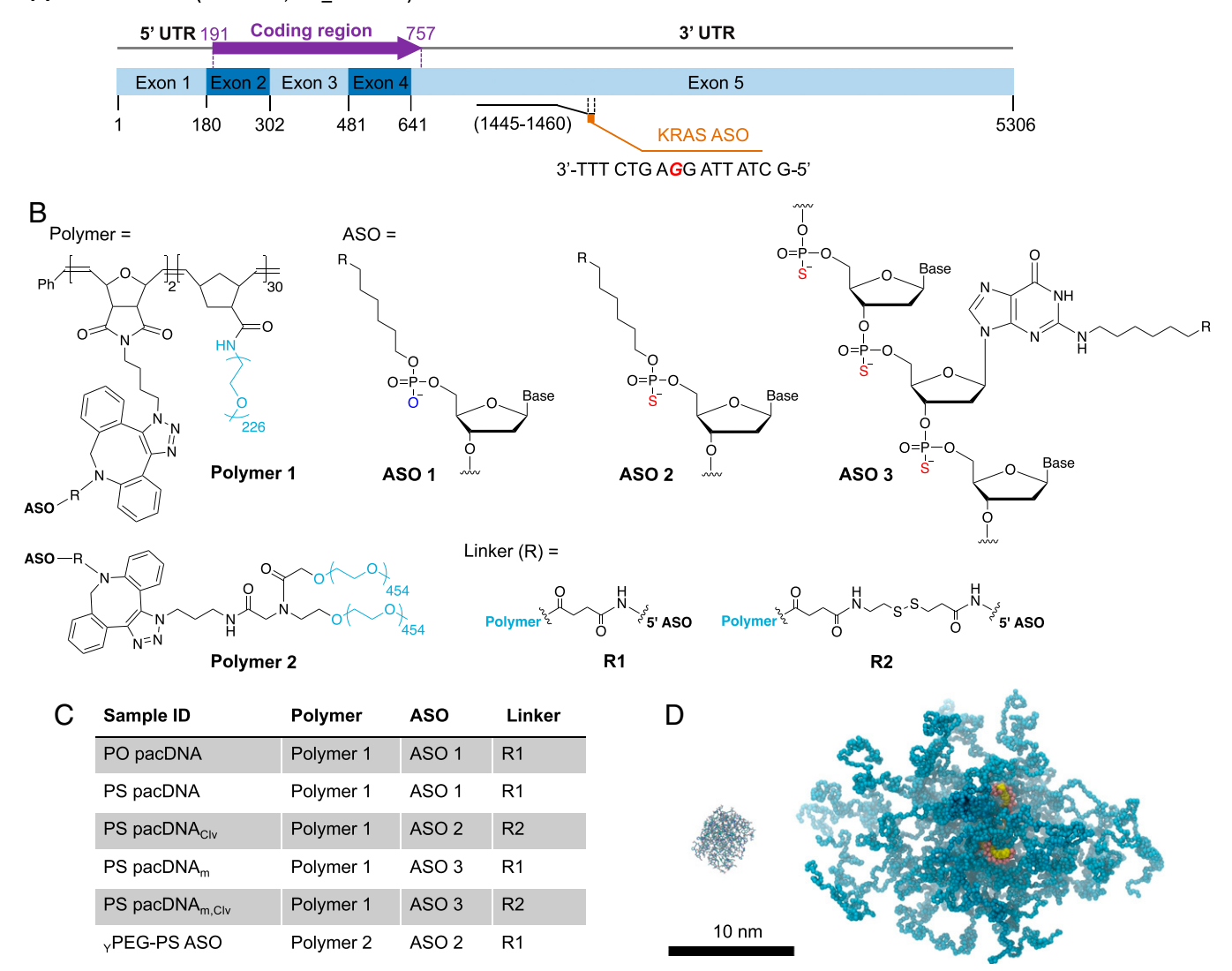


Fig. 1. Chemical and simulated structures of pacDNAs. (A) Antisense-targeted region of the KRAS mRNA. Highlighted deoxyguanosine (red) in the KRAS ASO sequence is used for midsequence conjugation to the bottlebrush polymer. (B) Polymer, ASO, and linker chemistry. (C) Sample ID and chemical structure. Clv: cleavable; m: midsequence conjugation; PO: phosphodiester; PS: phosphorothioate; PEG: Polymer 2. (D) A structural model from a coarse-grained molecular dynamics simulation of the pacDNA. A crystal structure of recombinant human DNase I is placed next to the pacDNA for size comparison.

The size is consistent with dynamic light scattering measurements, which show a number-average hydrodynamic diameter of ~30 nm in Nanopure water (SI Appendix, Fig. S3F). The redox responsiveness of pacDNAs with cleavable linkages was tested by treatment with 10 mM dithiothreitol (DTT) in phosphate-buffered saline (PBS) at 37 °C, a condition often adopted to mimic the reducing intracellular environment (SI Appendix, Fig. S3G). AGE shows that \sim 80% of the DNA is released after 30 min of treatment, as determined by gel densitometry analysis. In contrast, the same treatment for noncleavable pacDNAs resulted in no release of the DNA.

A hallmark feature of the pacDNA is its ability to hybridize with the complementary target in kinetically and thermodynamically the same manner as free DNA, but it is able to resist protein binding. We verified this feature using a fluorescence quenching assay, in which a quencher (dabcyl)-modified sense strand is added to fluorescein-labeled antisense pacDNA. Upon hybridization, the fluorescence is quenched due to the spatial proximity of the fluorophore-quencher pair, the rate of which is indicative of the hybridization kinetics (SI Appendix, Fig. S4A). All pacDNA

conjugates, the Y-shaped conjugate, and free ASO hybridize with the sense strand rapidly with a negligible difference (SI Appendix, Fig. S4B). When a scrambled dabcyl-DNA sequence was added, fluorescent signals were not affected, ruling out nonspecific binding. To investigate the extent of protein access, DNase I (an endonuclease mainly for double-stranded DNA) was added to prehybridized fluorophore/quencher-bearing duplexes. With DNase I action, an increase of fluorescence is expected, reflecting the nucleolytic degradation rate. As shown in *SI Appendix*, Fig. S4C, the phosphodiester (PO) pacDNA exhibits a significantly extended half-life $(t_{1/2})$ of \sim 92 min compared with free PO DNA, which is degraded rapidly with a $t_{1/2}$ of \sim 5 min. On the other hand, both the PS pacDNA and the naked PS ASO exhibit very limited enzymatic degradation, with 11.5% and 19.3% degraded after 10 h of treatment, respectively, which is in line with the typical nuclease resistance of PS oligonucleotides.

Cellular Uptake, KRAS Depletion, and Cell Viability. One of the most significant restraints to the use of ASOs for pharmacological purposes is their limited cellular uptake and localization

in the appropriate intracellular compartments (43). To investigate the cellular uptake of pacDNA, NCI-H358 cells (a KRAS^{G12C} NSCLC line) were treated with cyanine 3 (Cy3)labeled pacDNA or free ASO for 4 h in serum-free media. Oligonucleotides with natural PO internucleotide linkages typically do not traverse the lipophilic cell membrane passively due to their highly polyanionic nature (44). On the other hand, PS ASOs bind promiscuously to proteins (e.g., membrane and serum proteins), which ultimately results in high endocytosis but also increased the potential for off-target effects in vivo (26). Indeed, naked PS ASO exhibits ~30 times higher uptake rate by NCI-H358 cells compared with the PO ASO (Fig. 2 A and B). However, the PS pacDNA is internalized by the cells only ~1.6 times faster than PO pacDNA, and the latter is taken up ~10 times faster than the naked PO ASO (Fig. 2 A and B). We hypothesize that the bottlebrush polymer produces a "leveling" effect, which increases PO ASO uptake while reducing that of the PS ASO (both toward the intrinsic uptake level of the unmodified polymer). These results suggest that the brush polymer reduces the dependency on ASO chemistry for cellular uptake and can generate a more predictable uptake pattern irrespective of the ASO (Fig. 2 A and B and SI Appendix, Fig. S5 A and B). Confocal microscopy confirmed that in all cases the pacDNAs are internalized by the cell as opposed to

being surface bound (Fig. 2C and SI Appendix, Fig. S5C), although the punctate appearance of fluorescence signals suggests predominant distribution in endosomal structures. The presence of serum in cell culture media did not change these trends in cell uptake (SI Appendix, Fig. S5 D and E). To examine the uptake pathway, pharmaceutical endocytosis inhibitors were used to block the established pathways and their contribution was assessed using flow cytometry (SI Appendix, Table S2). The results indicate energy-dependent, mixed uptake mechanisms that likely involve macropinocytosis and clathrinmediated endocytosis (45, 46) (SI Appendix, Fig. S6).

To study the antisense activity of pacDNA and associated phenotypic response, two cell lines, NCI-H358 (KRAS G12C) and PC9 (wild type), were treated with pacDNAs and controls at concentrations ranging from 1 to 10 µM (ASO basis). Western blot of cell lysates shows dose-dependent down-regulation of KRAS for all pacDNA structures containing a correct ASO sequence, while a scrambled PS pacDNA and the bottlebrush polymer alone do not lead to apparent down-regulation (Fig. 2D and SI Appendix, Fig. S7). Target depletion is generally >50% irrespective of ASO chemistry, conjugation site, or releasability when the pacDNA concentration is greater than 5 µM. Notably, the pacDNAs exhibited stronger target depletion than the naked PS ASO, despite the latter showing the highest level of cellular

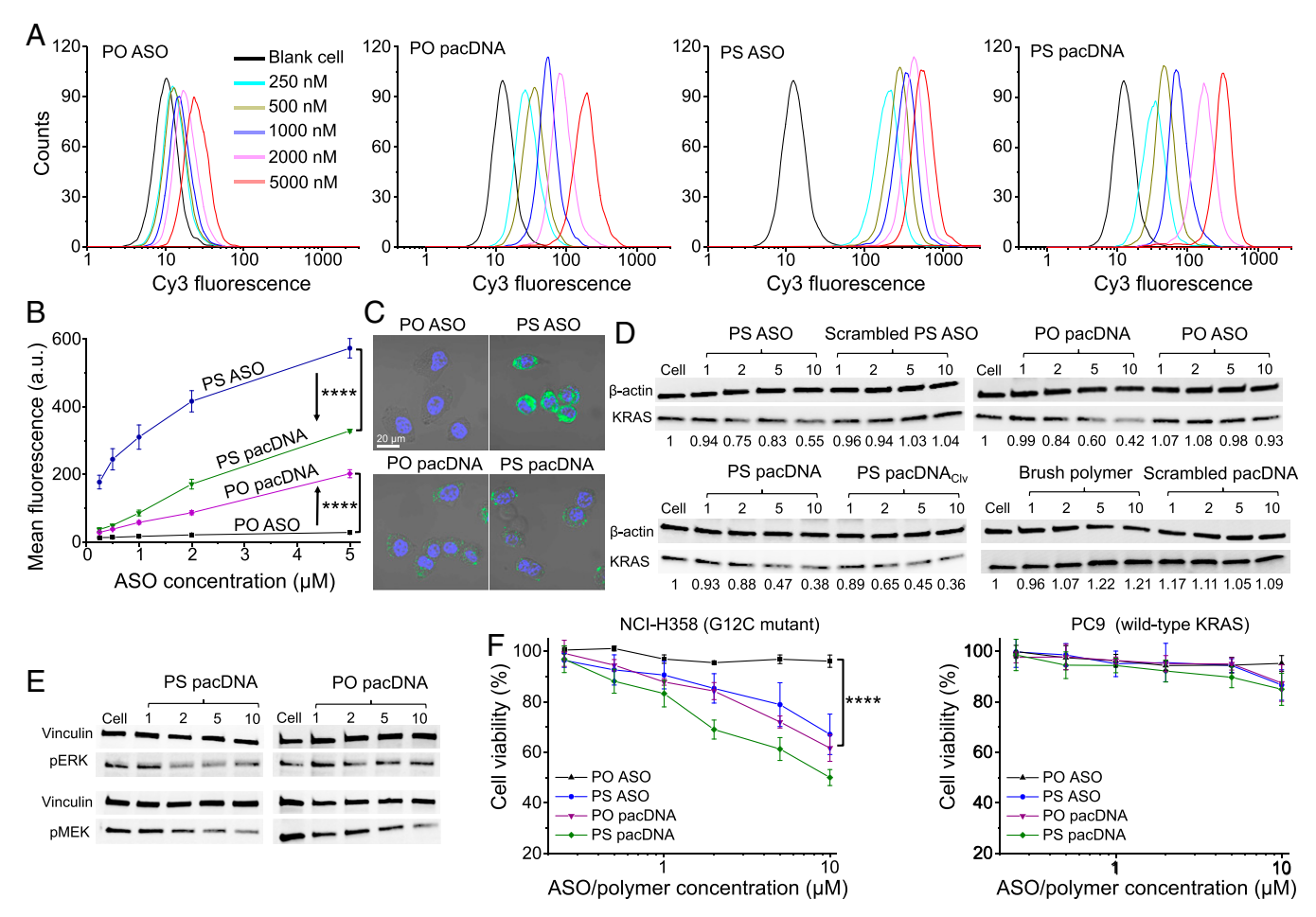


Fig. 2. Cellular uptake and phenotypic response in vitro. (A) Flow cytometry measurement of NCI-H358 cells treated with Cy3-labeled free ASOs (both PO and PS backbones) and corresponding pacDNAs (250 to 5,000 nM; ASO-basis) for 4 h. (B) Cellular uptake in NCI-H358 cells as indicated by mean cellular fluorescence, showing a "leveling" effect where the bottlebrush polymer reduces the uptake of normally high-uptake ASO but boosts that of low-uptake ASO. a.u., arbitrary units. (C) Confocal microscopy of NCI-H358 cells treated with fluorescently labeled PO or PS forms of molecular ASO and pacDNA. (D) Dosedependent depletion of KRAS in NCI-H358 cells by pacDNAs. (E) Western blot analysis of MAPK signaling in NCI-H358 cells after treatment with pacDNAs for 72 h. (F) Inhibitive effect in the proliferation of KRAS mutant cells (NCI-H358) vs. wild-type cells (PC9) by KRAS depletion using free ASOs and pacDNAs. Statistical analysis was performed using two-way ANOVA with Sidak's multiple comparison testing (****P < 0.0001).

uptake. While the pacDNAs were able to knock down KRAS in both cell lines, only NCI-H358 cells have shown significant dependency on KRAS for viability; the growth of PC9 cells is nearly unaffected by the treatment (Fig. 2F and SI Appendix, Figs. S8 and S9C), which is consistent with previous studies (11, 47). Among the pacDNA structures, the PS pacDNAs (PS pacDNA, PS pacDNA_{Clv}, and PS pacDNA_m) appear to be marginally more effective than the PO counterpart (PO pacDNA). The downregulation of KRAS in NCI-H358 cells was followed by inhibition of downstream mitogen-activated protein kinase (MAPK) pathway signaling including down-regulation of phosphor-MAPK kinase (pMEK) and phosphor-extracellular signal-regulated kinase (pERK) (Fig. 2E) and increased apoptosis (SI Appendix, Fig. S9A). FITC-annexin V/propidium iodide (PI) staining of cells treated with pacDNAs shows increased induction of apoptosis for all pacDNA variations (>22%), with the majority of the apoptotic cells in the early phase, while treatment with free PO DNA and the bottlebrush polymer does not result in appreciable changes relative to untreated cells. In addition, induction of procaspase-3 cleavage upon KRAS depletion was observed in a dose-dependent manner for NCI-H358 cells (SI Appendix, Fig. S9B). Collectively, these data suggest that pacDNA downregulates both mutant and wild-type KRAS isoforms and elicits selective phenotypic responses in *KRAS* ^{MUT} cells.

Plasma PK, Biodistribution, Antitumor Efficacy, and Safety. To assess the plasma PK of the pacDNA, blood samples from C57BL/6 mice dosed intravenously (i.v.) with Cy5-labeled pacDNA and controls were collected and analyzed for up to 72 h. Free ASOs are cleared rapidly via renal glomerular filtration with very short elimination half-lives ($t_{1/2\beta, PO} = 0.86 \text{ h}$, $t_{1/2\beta, PS} = 1.2 \text{ h}$; twocompartment model; Fig. 3A and SI Appendix, Table S3). In sharp contrast, all samples containing the bottlebrush polymers show markedly longer $t_{1/2\beta}$ (~14 to 23 h), among which the free polymer exhibits the greatest level of blood retention, with ~20% of the injected dose remaining in circulation at 72 h (Fig. 3A). Among the pacDNAs, three observations are made: 1) The stable, noncleavable pacDNAs (PO pacDNA, PS pacDNA, and PS pacDNA_m) show better plasma retention than the bioreductively cleavable counterparts (PS pacDNA_{Clv} and PS pacDNA_{m,Clv}); 2) the PS pacDNA is retained more than the PO pacDNA; and 3) midchain anchored pacDNA (PS pacDNA_m) circulates longer than the terminus-anchored version (PS pacDNA). These results suggest that the steric shielding by the bottlebrush polymer is not absolute; the enzymatic and chemical stability of the ASO as well as the level of its exposure to plasma components remain secondary contributing factors for PK. Nonetheless, the bottlebrush polymer decidedly elevates ASO blood concentration and bioavailability compared with naked ASOs with an improvement of one to two orders of magnitude if measured by the area under the curve (AUC $_{\infty}$).

One outcome of the elevated plasma PK is access to passive targeting of highly vascularized tissues such as certain tumors, likely via the enhanced permeation and retention effect. To assess the biodistribution of pacDNA and controls, BALB/C-nu/nu mice bearing subcutaneous NCI-H358 xenografts were injected i.v. with Cy5-labeled pacDNAs and controls. Fluorescence imaging of both live animals and the dissected organs 24 h postinjection confirms that free PO ASO is quickly and primarily cleared by the kidney, while the PS ASO is cleared by both the kidney and the liver, with weak signals at the tumor site (Fig. 3B and SI Appendix, Fig. S10). The Y-shaped PEG-PS ASO conjugate does not cause apparent changes in biodistribution relative to the parent ASO. Conversely, in stable pacDNA- and brush polymer-treated

mice, strong fluorescence signals are apparent throughout the entire animal body at 24 h, and tumor site accumulation is evident. Confocal microscopy of cryosectioned tumor slices reveals significant ASO signals not only on the periphery of the tumor but also within the depths of the solid tumor (Fig. 3D and SI Appendix, Fig. S11). It is found that the bioreductively cleavable conjugate (pacDNA_{m,Clv}) shows faster clearance and less tumor accumulation compared with the stable pacDNAs, possibly due to inadvertent release while in blood circulation, leading to liver/ renal clearance (SI Appendix, Fig. S10). We monitored the clearance of the samples from mice after a single i.v. injection by imaging the animals daily (*SI Appendix*, Figs. S12 and S13). The free bottlebrush polymer reached peak signal intensities 4 d after injection (Fig. 3B and SI Appendix, Fig. \$12), and the peak level persisted for 3 wk before slowly declining (SI Appendix, Fig. \$13). The tissue with the slowest clearance rate is the tumor, in which the bottlebrush polymer persisted for at least 13 wk (Fig. 3B and SI Appendix, Fig. S13). In comparison, both PO and PS pacDNA were cleared in 1 to 2 wk (still significantly enhanced relative to their parent ASOs; Fig. 3B and SI Appendix, Fig. S12). The PO pacDNA showed more pronounced tumorassociated fluorescence than the PS version, possibly because the PS ASO, even when shielded by the bottlebrush polymer, still retains a propensity for nonspecific binding with proteins, leading to recognition and uptake by the mononuclear phagocyte system. Indeed, fluorescence imaging of the dissected organs 2 wk postinjection shows that the PO pacDNA accumulates predominantly in the tumor, liver, and kidney, whereas the PS pacDNA exists in the highest abundance in the spleen and liver, followed by the tumor (Fig. 3C). Collectively, these data indicate that the bottlebrush polymer is a long-circulating, long-retention vector which can partially impart these properties to conjugated ASOs, making them viable for systemic delivery.

The antitumor efficacy of the pacDNA was assessed in male BALB/c nu/nu mice bearing subcutaneous NCI-H358 xenografts. When the xenografts reached a volume of ca. 100 mm³, pacDNAs, free ASOs, or vehicle (PBS) were administered i.v. (0.5 µmol/kg) once every third day for a total of 12 doses. By day 36, the average tumor volume in the vehicle-treated groups had progressed to ~900 mm³. Remarkably, all pacDNA structures triggered potent tumor growth inhibition (averaging 230 to 390 mm³; Fig. 4A and SI Appendix, Fig. S14A), irrespective of ASO conjugation site, chemical modification, and releasability. While the cleavable pacDNAs (PS pacDNA_{Clv} and PS pacDNA_{m,Clv}) appear to be slightly less potent than the stable forms (PO pacDNA, PS pacDNA, and PS pacDNA_m), statistical analysis shows the difference in tumor size among the pacDNA-treated groups to be insignificant. To rule out nonspecific antitumor activity from either the PS modification or the polymer component (or the enhanced tumor site delivery of PS oligonucleotides by the polymer), free PS ASO and a PS pacDNA with a scrambled sequence were used as negative controls; both resulted in insignificant antitumor response (Fig. 4A). Kaplan-Meier survival analysis (using an increase in tumor size of fourfold as a surrogate for survival endpoint; Fig. 4B and SI Appendix, Fig. S14B) shows that treatment with pacDNAs delays the time to reach the surrogate endpoint compared with the control groups. Immunohistostaining reveals that pacDNAs induced a marked reduction in KRAS protein levels in the tumor tissues after the last treatment (Fig. 4D and SI Appendix, Figs. S14C and S15). Consistently, histological analyses by hematoxylin and eosin (H&E) staining demonstrated severe loss of tumor cellularity in cases treated with KRAS-targeting pacDNAs compared with the cases from the control groups

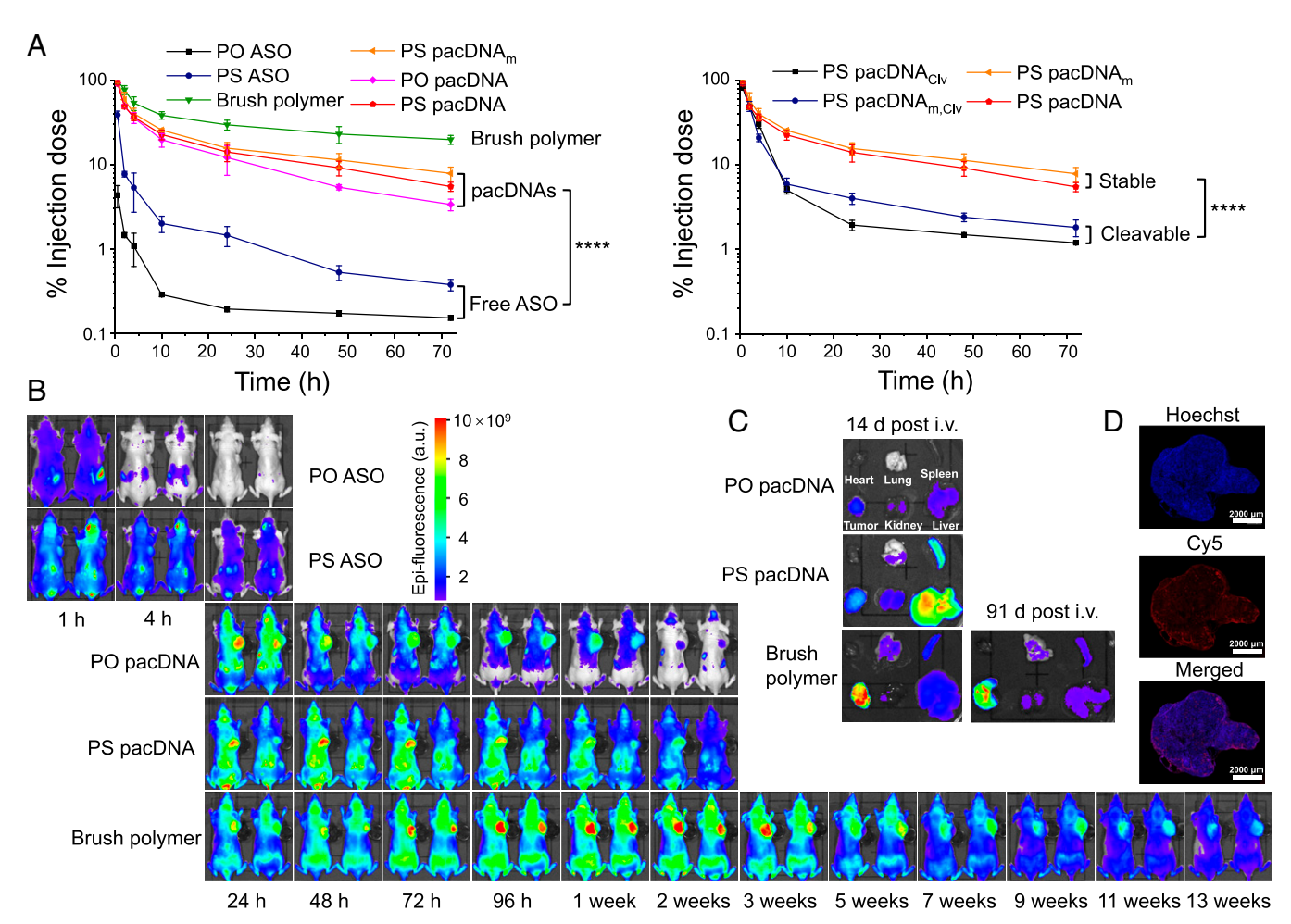


Fig. 3. Plasma PK and biodistribution in mice. (A) Plasma PK of pacDNAs, free ASO (both in PO and PS forms), and the bottlebrush polymer in C57BL/6 mice. (B) Fluorescence monitoring of i.v. injected Cy5-labeled pacDNAs and controls in BALB/c-nu mice bearing NCI-H358 xenograft. (C) Ex vivo imaging of tumors and other major organs 14 or 91 d postinjection. Imaging settings were kept identical. (D) Confocal microscopy of cryosectioned tumor tissue 24 h postinjection, showing tumor penetration (PS pacDNA). Statistical analysis was performed using two-way ANOVA with Tukey's multiple comparison testing. ****P < 0.0001.

(Fig. 4E and SI Appendix, Fig. S14D). These data strongly corroborate earlier in vitro indication that the pacDNA is able to relax the requirement on ASO chemistry, allowing natural, PO ASO to attain efficacy comparable to chemically modified ASOs. The results are particularly significant when one compares them with the preclinical evaluation of AZD4785 in an identical tumor model. The clinical ASO with cEt modification was able to reduce tumor growth to an extent very similar to the pacDNA. However, the overall dosage of the pacDNA throughout the treatment period is only 0.025 times that of AZD4785, which was dosed at 10 µmol/kg with a schedule of five subcutaneous injections per week (11).

To further explore the minimal effective dosage, a reduceddosage study was performed in which the pacDNAs were administered at 0.1 µmol/kg once every third day for a total of 12 i.v. injections. At 0.005 times the dosage of AZD4785, the pacDNAs (PO pacDNA, PS pacDNA, and PS pacDNA_m) are still able to produce a statistically significant phenotypic response, although a dose dependency in tumor size is evident (Fig. 4C). Notably, inhibition was not apparent until ~17 d into the treatment, which is possibly due to the accumulation of the pacDNA at the tumor site allowing for a critical concentration to be reached after several dosages. Overall, we attribute the massive increase in ASO bioactivity associated with the pacDNA to the improved PK and reduced nonantisense binding with proteins and cells.

To demonstrate the antitumor activities of the pacDNA against different mutant KRAS isoforms, a subcutaneous NCI-H1944 xenograft model, which carries the KRASG13D mutation, was established. In vitro studies with both the PS and the PO pacD-NAs confirm KRAS down-regulation and proliferation inhibition against NCI-H1944 cells, while the free PS ASO and the bottlebrush polymer show negligible inhibition (SI Appendix, Fig. \$16). Systemic delivery of the pacDNAs (PO and PS) to NCI-H1944 tumor-bearing mice resulted in potent tumor growth inhibition after 4 wk of i.v. injections at 2.0 µmol/kg every third day (Fig. 4F). Again, this dosage represents only 0.1 times that of AZD4785, with which the pacDNA was able to achieve a comparable level of antitumor response in an identical animal model. The treatment with the pacDNAs substantially delays the time to reach the surrogate survival endpoint, as determined by the Kaplan-Meier survival analysis (Fig. 4G). Immunohistostaining staining shows an apparent reduction in KRAS protein levels (SI Appendix, Fig. S17A). Reduced tumor cellularity was confirmed through H&E staining (SI Appendix, Fig. S17B). Throughout the 27-d treatment period, mice body weight for both the pacDNA- and control-treated groups remained constant (Fig. 4H). Collectively, these data demonstrate that systemic delivery of pacDNAs in preclinical models of KRAS^{MUT} NSCLC can achieve potent KRAS down-regulation and selective antitumor activity at a significantly lower dosage than what is previously possible, while using natural, unmodified oligonucleotides.

Treatment with pacDNA is well-tolerated in mice without apparent body weight loss or obvious changes in behavior (refusal to eat, startle response, etc.) (Fig. 4H and SI Appendix, Fig. S18).

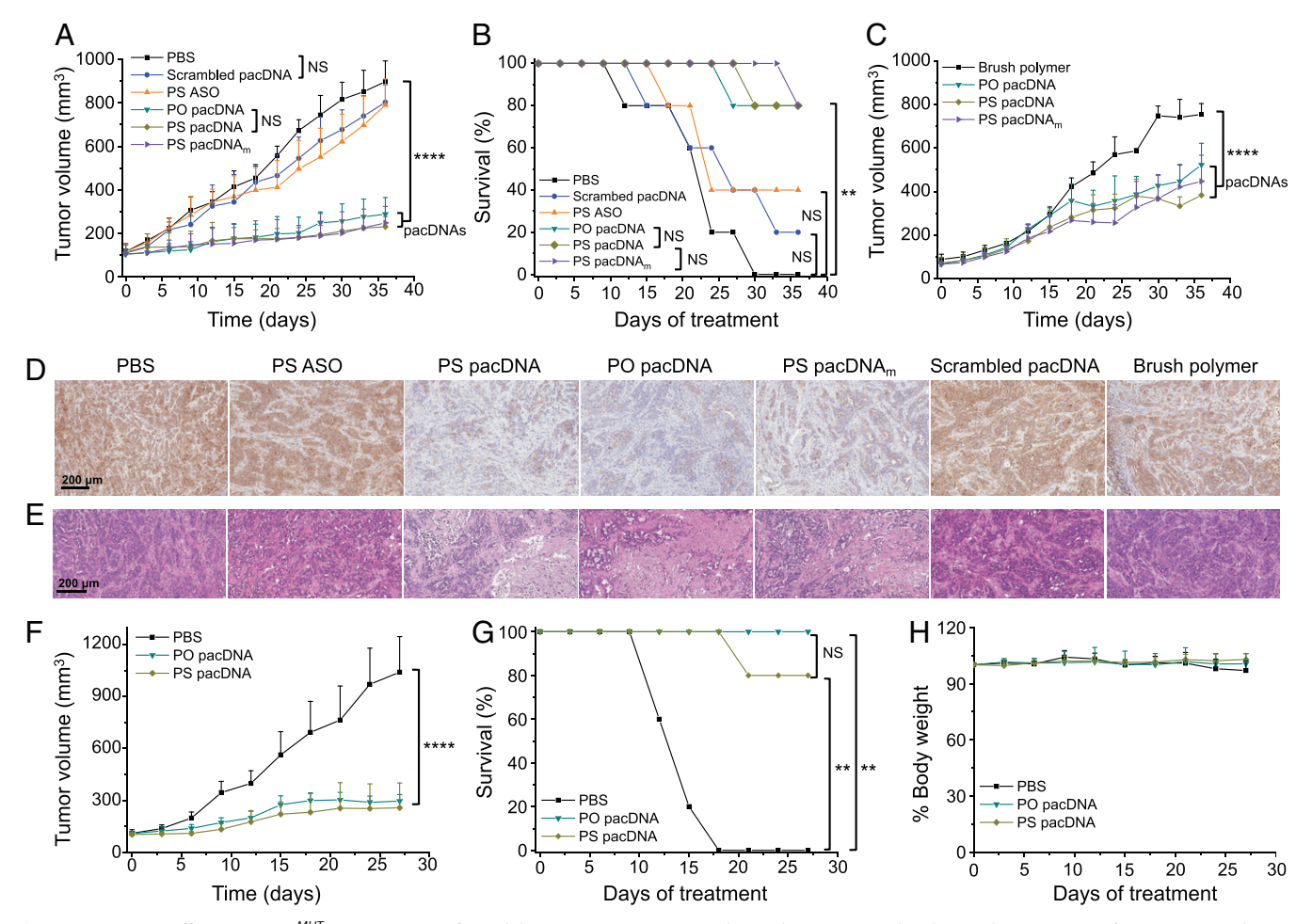


Fig. 4. Antitumor efficacy in KRAS^{MUT} NSCLC xenograft models. (A) NCI-H358 tumor volume changes in 36 d with i.v. administration of PBS, ASOs, and pacD-NAs at equivalent ASO doses (0.5 µmol/kg) every third day (treatment started on day 0). (B) Kaplan-Meier endpoint animal survival analysis for the NCI-H358 xenograft study. Data are shown as the percentage of remaining animals with tumors less than four times the initial starting volume in each treatment group. (C) Tumor growth inhibition of NCI-H358 xenografts at a reduced ASO dosage (0.1 µmol/kg). (D) Immunohistostaining of tumor cryosections, showing reduced KRAS expression in pacDNA-treated groups. (E) H&E staining of tumor tissues after the treatment period. (F) NCI-H1944 tumor volume changes with i.v. administration of PBS, PO pacDNA, and PS pacDNA at equivalent ASO doses (2.0 µmol/kg) every third day (treatment started on day 0). (G) Kaplan-Meier survival curves for NCI-H1944 tumor-bearing mice. Data are shown as the percentage of remaining animals with tumors less than four times the initial starting volume in each treatment group. (H) Body weight changes of NCI-H1944 tumor-bearing mice during the treatment period. For tumor inhibition, statistical analysis was performed using two-way ANOVA with Tukey's multiple comparison testing. For animal survival analysis, statistical significance was calculated by the log-rank test. ****P < 0.0001, **P < 0.01. NS, not statistically significant.

Histological staining of major organs (heart, spleen, liver, lung, and kidneys) with H&E shows no distinct variations between pacDNA- and vehicle-treated groups (SI Appendix, Figs. S19-S21). Oftentimes, gene vector materials (e.g., polycationic agents or surfactant-like materials such as micelles and liposomes) exhibit varying degrees of blood incompatibility, such as hemagglutination or hemolysis. The pacDNA, being noncationic and non-selfassembled, does not display noticeable hemolytic activity, as estimated by measuring the amount of the hemoglobin released from red blood cells (RBCs) under physiological conditions (Fig. 5A). For comparison, Lipofectamine 2000, a commercially available transfection agent, resulted in ~42% hemolysis to deliver an equivalent amount of ASO. In addition, liver indicators, including alanine aminotransferase (ALT), alkaline phosphatase (ALP), aspartate aminotransferase (AST), albumin, total bilirubin, and total protein, show no hepatic dysfunction associated with pacDNA (SI Appendix, Fig. S22). Renal function indexes (urea nitrogen and creatinine) as well as hematological parameters (globulin, cholesterol, glucose, calcium, phosphorus, chloride, potassium, sodium, and hemolysis and lipemia indices) are within normal ranges.

Unintended activation of the immune system was investigated in C57BL/6 mice following i.v. delivery of pacDNAs. Cytokines related to the innate and adaptive immunity (Fig. 5B and SI Appendix, Fig. S23), such as tumor necrosis factor α (TNF- α), interferon gamma (IFN- γ), and interleukin (IL)-1 α , IL-1β, IL-4, IL-6, IL-10, and IL-12 show no obvious changes as determined by enzyme-linked immunosorbent assays (ELISA). In contrast, lipopolysaccharide (LPS, positive control), induced strong expression of the majority of these cytokines. The anticarrier adaptive immunity following repeated dosages can be a significant difficulty for biopharmaceutical development, even with weakly antigenic carrier materials such as PEG, which leads to the accelerated blood clearance (ABC) phenomenon and increased hepatic/splenic accumulation (48). Rodent as well as large animal studies have illustrated that anti-PEG antibodies abolish the extended circulation times that PEG generally provides to conjugated therapeutics. Anti-PEG immunity may also result in serious complications beyond poor plasma PK, including hypersensitivity reactions, which can lead to anaphylaxis and death. To evaluate the anti-PEG immunoglobulin (Ig)M/IgG response and the potential ABC effect, repeated i.v. injections of pacDNAs (PO and PS) and free bottlebrush polymer were performed on healthy C57BL/6 mice at a dose of 0.5 µmol/kg (injections on the 1st, 4th, 11th, and the

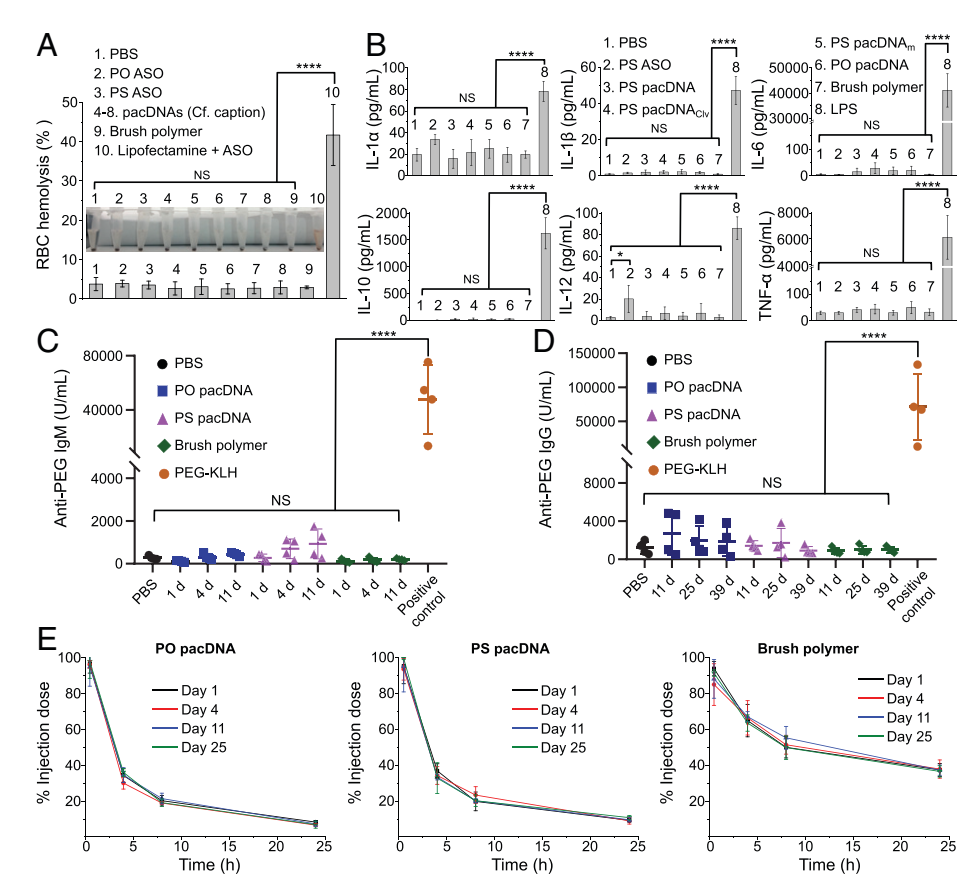


Fig. 5. Unwanted hemolytic and immunological activities of pacDNAs. (4) Hemolysis of human blood (type O+) treated with pacDNA and controls, as determined by spectrophotometric measurement of hemoglobin present in the supernatant of centrifuged RBC suspensions. The %RBC hemolysis is defined as the percentage of hemoglobin present in the supernatant compared with the total hemoglobin released by Triton X-100 treatment. (Inset) Photograph of centrifuged RBC suspensions. Sample identity for pacDNAs: 4. PO pacDNA, 5. PS pacDNA, 6. PS pacDNA_{Clv}, 7. PS pacDNA_m, 8. cytokine levels in the serum in C57BL/6 mice following injection of pacDNAs or controls. (C) Anti-PEG IgM levels and (D) anti-PEG IgG levels in the serum of C57BL/6 mice after repeated injections of pacDNAs and controls at timed intervals. (E) Repeated plasma PK measurements after four sequential i.v. administration of pacDNAs or free bottlebrush polymer in C57BL/6 mice. Plasma ASO or polymer levels were monitored after each injection. Statistical analysis was performed using one-way ANOVA with Tukey's multiple comparison testing. ****P < 0.0001, *P < 0.05. NS, not statistically significant.

25th day). The PS pacDNA induced a very limited anti-PEG IgM response, as measured on days 4 and 11 (Fig. 5C), whereas both pacDNA forms (but not the free polymer) produced an above-baseline level of IgG responses after 11 d (Fig. 5D). Both responses, however, are extremely weak compared with a positive control (PEG-keyhole limpet hemocyanin conjugate). Indeed, these anti-PEG antibody levels are insufficient to cause noticeable changes in plasma PK in subsequent injections of the pacDNA. As shown in Fig. 5E, blood clearance profiles of pacDNAs and the free bottlebrush polymer on days 1, 4, 11, and 25 are essentially identical. Remarkably, the low PEG antigenicity appears to be unique to the pacDNA structure. When pacDNAs (both PO and PS), brush polymer, or yPEG-PS ASO were regularly given i.v. to C57BL/6 mice (12 injections over 36 d, 0.5 µmol/kg), the yPEG-PS ASO-treated group developed very high IgM and IgG antibody titers 7 and 14 d after the last injection, respectively, but no apparent anti-PEG antibodies were detected in the pacDNA- and brush polymer-treated groups (SI Appendix, Fig. S24). Taken together, our results suggest that the pacDNAs are well-tolerated in mice, and the platform is generally safe without significant acute toxic and immunogenic shortcomings.

Discussion

A sound rationale and clinical validation for targeting KRAS have emerged for the treatment of cancer, but other than the G12C mutant, KRAS has remained undruggable. Methodologies to deplete oncogenic KRAS using nucleic acids and derivatives such as ASO and siRNA molecules have been developed. However, these approaches are limited by inefficient delivery, resulting in increased dosage requirements and side effects associated with off-target binding, unnatural nucleotide analogs, and unwanted immune system activation. Our results with the pacDNAs demonstrate that the molecular brush-conjugated ASO against KRAS mRNA markedly increases the potency of the ASO in vivo while suppressing nearly all side effects, which critically elevates the translational potential of the antisense approach to the KRAS

Three unique properties of the pacDNA are important for its clinical feasibility. First, the pacDNA is a selective form of oligonucleotide therapeutics. Unlike traditional ASO delivery systems, the pacDNA is a molecular agent that remains hybridizable to target strands without the ASO being separated from the polymer. Our data demonstrate that the binding kinetics and thermodynamics of pacDNA structures are almost indistinguishable from that of free DNA. Thus, the pacDNA is more akin to a selective form of DNA that resists protein binding than a traditional drug delivery vehicle. Because almost all cases of unwanted, nonantisense side effects are preceded by protein recognition of the oligonucleotide, be it degradation, TLR activation, and inhibition of the coagulation cascade, the selectivity of the pacDNA translates into greater in vivo efficiencies with reduced potential for adverse effects. Second, the pacDNA simultaneously enhances transfection efficiency and in vivo

properties. Conventional vectors often face an activity-toxicity dilemma: Efforts to improve cellular transfection efficiency frequently result in poorer biopharmaceutical properties such as increased uptake by the mononuclear phagocyte system, clearance, and toxicity. The pacDNA, in contrast, resists opsonization and is not strongly recognized by phagocytic cells, allowing for significantly improved plasma PK and biodistribution parameters, including elimination half-life, blood availability, and passive targeting of nonliver parenchymal organs. In addition, the pacDNA exhibits a moderate level of cellular uptake and reasonable antisense potency. This combination allows the pacDNA to be used at a much lower dosage, which provides more flexibility in designing effective therapeutic oligonucleotides by circumventing toxicity constraints. Third, the pacDNA is designed with safety and clinical translatability first and foremost. The core of the pacDNA is a noncationic bottlebrush polymer consisting mainly of the widely used, biocompatible polymer PEG, which is recognized as generally safe for pharmaceutical use. A novel mechanism of steric compaction (as opposed to complexation, encapsulation, or chemical modification) is used to protect the oligonucleotide and facilitate delivery, which annuls the potential negative effects associated with polycationic, liposomal, or chemically modified agents. Of note, while the pacDNA exhibits an encouraging efficacy and safety profile, it may be desirable to have tunable degradability built into the bottlebrush polymer backbone as a means to control clearance. Toward this goal, degradable materials may be adopted, including novel ROMP polymers developed by Johnson, condensation polymers with a nonaliphatic backbone, and miktoarm star polymers/nanoparticles, as long as the high-density PEG environment characteristic of the pacDNA is retained (49-53).

In summary, our studies show that the molecular brush enhances the delivery of conjugated ASOs in suppressing oncogenic KRAS in vivo, which massively reduces the dosage level required for a phenotypic response compared with naked ASOs. Importantly, the pacDNA relaxes the requirement of ASO modification chemistry, which allows natural, unmodified nucleic acids to be used in place of chemically modified ASOs, bypassing their potential toxicity. The bottlebrush polymer also contributes significantly to the diminished clearance from systemic circulation and the enhanced tumor accumulation, while itself generating no apparent adverse toxic or immunogenic side effects. Collectively, our results highlight the potential of pacDNA as an antisense agent that directly targets the highly unmet clinical need represented by KRAS-driven human cancers. Further, the general platform serves as a single-entity alternative to current paradigms in oligonucleotide therapeutics, including modified oligonucleotides and formulations with liposomes/ lipid nanoparticles.

Materials and Methods

Oligonucleotide Synthesis. Oligonucleotides (both PO and PS versions) used in this work were synthesized on a model 391 DNA synthesizer (Applied Biosystems, Inc.) using standard solid-phase phosphoramidite methodology. DNA strands were cleaved from the CPG support using ammonium hydroxide (28% NH₃ in H₂O) at room temperature for 24 h and purified by reverse-phase highperformance liquid chromatography (HPLC). The dimethoxytrityl protecting group was removed by treatment with 20% acetic acid in H₂O for 1 h, followed by extraction with ethyl acetate three times. Upon purification, DNA was stored at $-20\,^{\circ}\text{C}$. To synthesize the dye-labeled DNA, 3'-(6-fluoresecein) CPG, Cy3 CPG, and cyanine 5 (Cy5) CPG were used to synthesize the antisense strands. The 5' dibenzocyclooctyl (DBCO) groups were incorporated by using 5'-DBCO-TEG phosphoramidite. To synthesize DBCO-SS-DNA, purified 5' amine-modified DNA (100 nmol) was dissolved in 100 µL of NaHCO₃ (0.1 M) buffer, to which

0.5 mg dibenzocyclooctyne-SS-N-hydroxysuccinimidyl ester (DBCO-SS-NHS) was added via 100 μL dimethyl sulfoxide (DMSO) solution. The reaction mixture was shaken at 0 °C overnight. The products (DBCO-SS-DNA) were purified by reverse-phase HPLC. To install midsequence DBCO groups, amine-modified DNA strands were first synthesized using an amino modifier (amine-C6 dG), which were then reacted with DBCO-NHS or DBCO-SS-NHS in 0.1 M bicarbonate solution overnight at 4 $^{\circ}$ C. The reaction mixture was passed through a NAP-10 column (GE Healthcare) and then purified using the reverse-phase HPLC. The successful syntheses of all oligonucleotides in this work were confirmed by matrix-assisted laser desorption/ionization time-of-flight mass spectrometry.

Synthesis of Azide-Functionalized Bottlebrush Polymer. Two monomers, norbornenyl bromide and norbornenyl PEG, were synthesized following previously reported procedures (33). Modified second-generation Grubbs catalyst was prepared based on a published method shortly prior to use (54). Next, norbornenyl bromide (5 eq) was dissolved in deoxygenated dichloromethane under N₂ and cooled to -20 °C in an ice-salt bath. The modified Grubbs' catalyst (1 eq) in deoxygenated dichloromethane was added to the solution via a gastight syringe, and the solution was stirred vigorously for 30 min. After thin-layer chromatography confirmed the complete consumption of the monomer, norbornenyl PEG (50 eq) in deoxygenated dichloromethane was added to the reaction, and the mixture was stirred for 6 h. Several drops of ethyl vinyl ether were added to quench the reaction and the solution was stirred for an additional 2 h. After concentration under vacuum, the residue was precipitated into cold diethyl ether three times. The precipitant was dried under vacuum to afford a dry powder. Subsequently, the resulting brush polymer was treated with an excess of sodium azide in anhydrous dimethylformamide (DMF) overnight at room temperature. The materials were transferred to a dialysis tubing (molecular weight cutoff: 10 kDa), dialyzed against Nanopure water for 24 h, and lyophilized to afford a white, dry powder. The successful incorporation of azide functionalities was confirmed via FT-IR. The number of azide groups per copolymer available for coupling was estimated by reacting with alkyne-modified fluorescein and subsequent comparison of the fluorescence with a standard curve established with free fluorescein. The final polymer was characterized by ¹H NMR and DMF gel permeation chromatography (GPC) (SI Appendix, Fig. S2).

Synthesis of Azide-Functionalized Y-Shaped PEG. Y-shaped PEG NHS ester (1 eq), 3-azido-1-propanamine (2 eq), and N, N-diisopropylethylamine (2 eq) were dissolved in anhydrous dichloromethane and added to a round-bottom flask. The reaction mixture was stirred overnight at room temperature and precipitated into diethyl ether three times. The product was purified by a NAP-10 column and lyophilized as a white power with a recovery yield of 80%.

Synthesis of Cy5-Labeled Bottlebrush Polymer. The bottlebrush polymer was labeled with Cy5 via copper-catalyzed click chemistry for in vivo fluorescence tracking. The polymer (30 mg, 100 nmol) in Nanopure water (3 mL) was added with Cy5-alkyne (110 nmol, 110 μL 1 mM DMSO solution). The catalyst system (CuSO₄·5H₂O, 80 nmol; Tris-hydroxypropyltriazolylmethylamine, 100 nmol; sodium ascorbate, 500 nmol) was added to the solution and stirred at room temperature for 12 h. The reaction mixture was dialyzed against Nanopure water and further purified using agueous GPC. The fractions containing the conjugate were collected, concentrated, desalted, and lyophilized to afford a blue powder. UV-visible spectroscopy indicates that there was ~1.0 Cy5 dye molecule per polymer.

Synthesis of pacDNAs. In a typical procedure, azide-functionalized brush copolymers (15 mg, 50 nmol) were dissolved in 500 µL agueous NaCl solution (2 M), to which DBCO-modified DNA (100 nmol) in 200 μL aqueous NaCl solution (2 M) was added (2 eq to N₃). The reaction mixtures were shaken gently for 24 h at 50 °C on an Eppendorf Thermomixer. The conjugates were purified using aqueous GPC to remove the unreacted DNA. Thereafter, the collected fractions were concentrated, desalted with a NAP-25 column, and lyophilized to yield a white powder (or green/red/blue powders for fluorescein-, Cy3-, and Cy5-labeled conjugates, respectively). To synthesize _YPEG-DNA conjugate, 2 mg (50 nmol) of Y-shaped PEG-azide was mixed with 60 nmol DBCO-modified DNA strands in 200 µL aqueous NaCl solution (2 M). The reaction mixture was shaken at 50 °C for 24 h and purified by reverse-phase HPLC. After purification, the conjugate was desalted by a NAP-10 column and lyophilized to yield a white powder.

Molecular Dynamics (MD) Simulation. MARTINI coarse-grained (CG) force field was used for MD simulation of pacDNA in explicit solvation by water and neutralizing sodium ions (55). The force field incorporates four heavy atoms with similar chemical identities into one CG bead and therefore reduces the freedoms of the molecules needed to calculate. Bonded parameters are defined based upon molecular structure, while nonbonded parameters, including van der Waals and electrostatic forces, are derived from free energy partitioning between polar and organic solvents. The MARTINI version of PEG was developed by Lee et al. (56). The atomistic to CG mapping is 3:1 for the PEG monomer. This mapping ratio deviates from the standard MARTINI mapping scheme due to the size of the PEG monomer. Herein, the PEG monomer is represented by an SNO particle in the CG force field. The parameters for the Lennard-Jones interaction between PEG and water are $\sigma = 0.47$ nm and $\epsilon = 4.0$ kJ/mol. The time step of CG MD simulations was set to be 0.010 ps. Periodic boundaries conditions were used in all directions. The system was controlled using an NPT ensemble. The temperature was controlled at 310 K using the Berendsen thermostat while the pressure was controlled at 1 atm using the Berendsen barostat (57). The cutoff distances of van der Waals and short-range electrostatic interactions were set at 1.2 nm. Long-range electrostatic interactions were not considered. All simulations were performed using the GROMACS 2018 package (58).

Hybridization and Nuclease Degradation Kinetics. For hybridization kinetics, fluorescein-labeled pacDNA and controls were dissolved in PBS buffer (pH 7.4) at a final DNA concentration of 100 nM. Each sample (1 mL) was transferred to a fluorescence cuvette, to which dabcyl-labeled complementary strand or noncomplementary dummy strands (2 eq) were added via 2 µL of PBS solution. The solution was rapidly mixed with a pipette. The fluorescence of the solution (excitation = 494 nm, emission = 522 nm) was continuously monitored before the mixing and every 3 s thereafter using a Cary Eclipse fluorescence spectrometer. The endpoint was determined by adding a large excess (10 eq) of the complementary dabcyl-DNA to the mixture, followed by incubation for 2 h. The kinetics plots were normalized to the endpoint determined for each sample, and the reported values are the average of three independent experiments.

For nuclease degradation, pacDNA and controls (1 µM DNA basis; fluorescein-labeled) were each mixed with their complementary dabcyl-labeled DNA (2 μM) in PBS buffer. The solutions were gently shaken at room temperature overnight. Subsequently, 100 µL of each sample was withdrawn and diluted to 100 nM with assay buffer (50 mM Tris·HCl, 50 mM NaCl, and 20 mM MnCl₂, pH = 7.5), to which DNase I (0.1 unit/mL) was added and rapidly mixed. The fluorescence of each sample was monitored before the addition of DNase I and every 3 seconds thereafter (excitation = 494 nm, emission = 522 nm) for 10 h. The endpoint of each sample was determined by measuring the fluorescence of pacDNAs or controls at an identical concentration in the absence of the dabcyl-labeled complementary strand. The kinetics plots were normalized to the endpoints of each sample, and the reported values are the average of three independent experiments.

DNA Release In Vitro. Conjugates (PS pacDNA, PS pacDNA_m, PS pacDNA_{Clv}, and PS pacDNA_{m.Clv}, 100 nM) were mixed with 10 mM DTT in 1× PBS at 37 °C for 1 h. Thereafter, the solutions were subject to agarose gel electrophoresis using 1% agarose gel in 0.5× TBE buffer with a running voltage of 120 V. The amount of DNA released was determined using band densitometry analysis. The experiment was conducted in triplicates.

Cell Culture, Flow Cytometry, and Confocal Microscopy. Cells were cultured in RPMI 1640 supplied with 10% fetal bovine serum (FBS), 1% L-glutamine, and 1% antibiotics at 37 °C in a humidified atmosphere containing 5% CO₂. Cellular uptake of pacDNAs and controls was evaluated using flow cytometry and confocal laser scanning microscopy. For flow cytometry, cells were seeded in 24-well plates at a density of 2.0×10^5 cells per well in 1 mL full growth medium and cultured for 24 h at 37 °C with 5% CO2. After washing by PBS twice, Cy3-labeled pacDNAs and controls (250 nM to 5 μ M eq of ASO) dissolved in RPMI culture medium (either serum-free or with 10% FBS) was added, and cells were further incubated at 37 °C for 4 h. Subsequently, cells were washed with PBS three times and suspended by treatment with trypsin. Thereafter, 2 mL of PBS was added to each culture well, and the solutions were centrifugated for 5 min (1,000 rpm). Cells were then resuspended in 0.5 mL of PBS for flow cytometry analysis on a BD FACS Calibur flow cytometer. Data for 1.0×10^4 gated events were collected.

For confocal microscopy, cells were seeded in 24-well glass bottom plates at a density of 1.0×10^5 cells per well and cultured in 1 mL complete culture medium for 24 h at 37 °C. After washing by PBS twice, Cy3-labeled pacDNAs and controls (250 nM to 5 μ M eq of ASO) dissolved in RPMI culture medium (either serum-free or with 10% FBS) was added, and cells were further incubated at 37 °C for 4 h. Thereafter, cells were washed with PBS three times and fixed with 4% paraformaldehyde for 30 min at room temperature, followed by another three washings with PBS. The cells were then stained with Hoechst 33342 for 10 min and imaged on an LSM-700 confocal laser scanning microscope (Carl Zeiss Ltd.). Imaging settings were kept identical for all samples in each study.

Pharmacological Inhibition of Cellular Uptake. To study the cellular internalization pathway, NCI-H358 cells (2.0×10^5) were seeded into 24-well plates and incubated at 37 °C overnight for cells to settle down. The cells were pretreated with rottlerin (1 or 3 µg/mL), methyl-β-cyclodextrin (2.5 or 12.5 mg/mL), chloropromazine (1 or 5 µg/mL), or sodium azide (NaN₃, 10 or 50 mM) for 30 min, before being further incubated with 2 μ M Cy3-labeled pacDNAs or free PS ASO for 4 h. The inhibitor concentrations were maintained in the cell culture medium throughout the experiments. Thereafter, the cells were washed with PBS three times and harvested by trypsinization. All samples were analyzed by flow cytometry (FACS Calibur; BD Bioscience) to determine the extent of cellular internalization. All measurements were performed in triplicates and the results were averaged.

MTT Cytotoxicity Assay. The cytotoxicity of free ASOs, bottlebrush polymer, and pacDNAs was evaluated with the MTT (dimethylthiazol-diphenyltetrazolium bromide) colorimetric assay for NCI-H358, NCI-H1944, and PC9 cells. Briefly, 1.0×10^4 cells were seeded into 96-well plates in 200 μL Dulbecco's modified Eagle's medium per well and were cultured for 24 h. The cells were then treated with pacDNAs and controls at varying concentrations of ASO or polymer (0.25 through 10 µM; ASO basis). Cells treated with vehicle (PBS) were set as a negative control. After 48 h of incubation, 20 µL of 5 mg/mL MTT stock solution in PBS was added to each well. The cells were incubated for another 4 h, and the medium containing unreacted MTT was removed carefully. The resulting blue formazan crystals were dissolved in DMSO (200 µL per well), and the absorbances (490 nm) were measured on a BioTek Synergy Neo2 Multi-Mode microplate reader (BioTek Inc.).

Hemolytic Activity Assay. A hemoglobin-free RBC (2% wt/vol) suspension was prepared by repeated centrifugation (2,000 rpm for 10 min at 4 °C) and resuspension in ice-cold PBS for a total of three times. After the final resuspension, the concentration of RBCs was adjusted to 2% wt/vol. Thereafter, samples and controls were dissolved in PBS, added to the RBC suspension in 1:1 (vol:vol) ratio, and incubated for 1 h at 37 °C. Complete hemolysis was attained using 2% vol/vol Triton-X, yielding the 100% control value. After incubation, centrifugation (2,000 rpm for 10 min at 4 °C) was used to isolate intact RBCs, and the supernatants containing released hemoglobin were transferred to quartz cuvettes for spectrophotometric analysis at 545 nm. Results were expressed as the amount of hemoglobin released as a percentage of total. All measurements were performed in triplicates and the results were averaged.

Western Blot Analysis. Cells (NCI-H358, NCI-H1944, or PC9) were plated at a density of 2.0×10^5 cells per well in 24-well plates in RPMI medium and cultured overnight at 37 °C with 5% CO₂. Thereafter, samples and controls (1 to 10 μM eq ASO) in serum-free media were added to the wells and incubated with the cells for 4 h, before serum was added to the incubation mixture. Cells were cultured for another 68 h. Thereafter, cells were harvested and whole cell lysates were collected in 100 µL of RIPA Cell Lysis Buffer with 1 mM phenylmethanesulfonylfluoride (Cell Signaling Technology, Inc.) following manufacturer's protocol. Protein content in the extracts was quantified using a bicinchoninic acid protein assay kit (Thermo Fisher). Equal amounts of proteins (30 µg per lane) were separated on 4 to 20% gradient sodium dodecyl sulfate polyacrylamide gel electrophoresis and electrotransferred to nitrocellulose membrane. The membranes were then blocked with 3% bovine serum albumin in Trisbuffered saline supplemented with 0.05% Tween-20 and further incubated with appropriate primary antibodies overnight at 4 °C. After washing and incubation with secondary antibodies, detected proteins were visualized by chemiluminescence using the ECL Western Blotting Substrate (Thermo Scientific). Antibodies used for Western blots were KRAS antibody (NBP2-45536; Novus Biologicals), β-actin (AM4302), vinculin clone hVIN-1 (V9131; Sigma-Aldrich), phospho-ERK1/2 clone E10 (T202/Y2014; 9106), phospho-MEK1/2 clone 41G9 (S218/S222; 9154), caspase 3 (9668), anti-rabbit IgG, HRP-linked antibody (7074P2), and antimouse IgG, HRP-linked antibody (7076S). Unless otherwise noted, antibodies were obtained from Cell Signaling Technologies. Western blot images were quantified using the ImageJ software by comparing the detected protein band with that of the housekeeping protein.

Flow Cytometric Analysis of Apoptosis. Cells were plated at a density of 2.0×10^5 cells per well in 24-well plates in RPMI medium and cultured overnight at 37 °C with 5% CO₂. Thereafter, samples and controls (10 μM eq ASO) in culture media were added to the wells and incubated with the cells for 48 h. Apoptotic cells were determined using annexin V-fluorescein isothiocyanate (FITC)/PI apoptosis staining kit according to the manufacturer's instructions (KA3805; Abnova). Data were acquired using a FACS Calibur (BD Biosciences). All experiments were performed independently three times.

Animal Studies. All mouse studies were approved by the Institutional Animal Care and Use Committee of Northeastern University and carried out under pathogen-free conditions in the animal facility of Northeastern University and in accordance with National Institutes of Health animal care guidelines. The animals had free access to sterile food pellets and water and were kept in the laboratory animal facility with temperature and relative humidity maintained at 23 ± 2 °C and $50 \pm 20\%$, respectively, under a 12-h light/dark cycle. Mice were kept for at least 1 wk to acclimatize them to the food and environment of the animal facility prior to experiments.

Plasma PK. Immunocompetent mice (C57BL/6) were used to examine the plasma PK of free ASO (both PS and PO), Y-shaped PEG (40 kDa)-ASO conjugate, pacDNAs, and free bottlebrush polymer lacking an ASO component. Mice were randomly divided into nine groups (n = 4). Cy5-labeled samples were i.v. administrated via the tail vein at equal ASO dosage (0.5 µmol/kg; free polymer concentration equals that of the pacDNAs). Of note, the fluorescence label is located on the ASO component except for the free polymer. Blood samples (25 μL) were collected from the submandibular vein at varying time points (30 min and 2, 4, 10, 24, 48, and 72 h) using BD Vacutainer blood collection tubes with lithium heparin. Heparinized plasma was obtained by centrifugation at 3,000 rpm for 15 min, aliquoted into a 96-well plate, and measured for fluorescence intensity on a BioTek Synergy HT plate reader (BioTek Instruments Inc.). The amounts of ASO in the blood samples were estimated using standard curves established for each sample. To establish the standard curves, samples of known quantities were incubated with freshly collected plasma for 1 h at room temperature before fluorescence was measured.

NCI-H358 Xenograft Tumor Model Preparation. To establish the NCI-H358 xenograft tumor model, $\sim 4 \times 10^6$ cells in 100 μ L PBS were implanted subcutaneously on the right flank of 6-wk-old BALB/c nude mice. Mice were monitored for tumor growth every other day.

Whole-Animal and Ex Vivo Organ Imaging. NCI-H358 xenograft-bearing BALB/c nude mice were i.v. injected with Cy5-labeled samples at an ASO dose of 0.5 µmol/kg animal weight and were scanned at 1, 4, 8, and 24 h and daily thereafter until 13 wk or until fluorescence was no longer observable using an IVIS Lumina II imaging system (Caliper Life Sciences, Inc.). To evaluate the biodistribution of pacDNAs and the bottlebrush polymer, mice were killed using CO₂, and major organs and the tumor were removed for biodistribution analysis. For the analysis of tumor penetration depth, tumors were immediately frozen in optimum cutting temperature compound (Fisher Scientific Inc.) 24 h after injection. The frozen tumor tissues were cut into 8-µm-thick sections using a cryostat, stained with Hoechst 33342, and imaged on an LSM-880 confocal laser scanning microscope (Carl Zeiss Ltd.).

Antitumor Efficacy in NCI-H358 Xenograft-Bearing Mice. To screen the pacDNA variants in antitumor efficacy, an NCI-H358 subcutaneous xenograft model was first established. When the xenograft reached a volume of ca. 100 mm³, mice were randomly divided into 12 groups (n = 5) to receive the following via the tail vein: 1) PBS, 2) PO pacDNA (0.1 μmol/kg), 3) PS pacDNA (0.1 μmol/kg), 4) PS pacDNA_m (0.1 μmol/kg), 5) free PS ASO (0.5 μmol/kg), 6) PO pacDNA (0.5 µmol/kg), 7) PS pacDNA (0.5 µmol/kg), 8) PS pacDNA_{Clv} (0.5 μ mol/kg), 9) PS pacDNA_m (0.5 μ mol/kg), 10) PS pacDNA_{m,Clv} (0.5 μ mol/kg), 11) scramble PS pacDNA (0.5 µmol/kg), or 12) free bottlebrush polymer (0.5 µmol/kg). Samples were injected once every 3 d until day 36. The volume of tumors and weight of mice were recorded before every treatment and 3 d after the last treatment. Antitumor activity was evaluated in terms of tumor size by measuring two orthogonal diameters at various time points ($V = 0.5 \times ab^2$; a: long diameter, b, short diameter). At day 36, mice were killed with CO2, and tumors and major organs (heart, lung, liver, spleen, and kidney) from each group were excised, fixed in 4% paraformaldehyde/PBS for 6 h, and placed into a 30% sucrose/PBS solution overnight at 4 °C. The fixed tissues were paraffinembedded and cut into 8-µm-thick sections with a cryostat. The sections were then processed with H&E staining. Immunohistochemistry staining of KRAS was carried out using mouse anti-KRAS primary antibody (1:1,000 dilution, Invitrogen) and goat anti-mouse secondary antibody (1:5,000 dilution, Thermo

Antitumor Efficacy in NCI-H1944 Xenograft-Bearing Mice. Eight-week-old male athymic nude mice (n = 5) were injected subcutaneously with ca. 5×10^6 NCI-H1944 cells in 100 μ L PBS on the right flank. When the mean tumor volume reached ~100 mm³, the tumor-bearing animals were treated i.v. with PBS, PO pacDNA, or PS pacDNA at 2.0 µmol/kg animal weight via the tail vein once every 3 d for 27 d. The volume of tumors and weight of mice were recorded before every treatment and on the third day after the last treatment. After that, the animals were killed by CO₂, and tumor samples were collected for immunohistochemical analysis. Main organs (lung, heart, liver, kidney, and spleen) were collected to assess toxicity through histological analysis.

Blood Biochemistry. Healthy C57BL/6 mice (6 to 8 wk, n=4) were injected i.v. with PO pacDNA, PS pacDNA, PS ASO, and free bottlebrush polymer three times a week for 2 wk with the equal DNA or brush polymer dose of 0.5 µmol/kg animal weight. Blood samples were collected from the submandibular vein 24 h after the last injection, allowed to clot by being left undisturbed for 30 min, and centrifuged at 3,000 rpm for 5 min, and the serum was collected. Serum AST, ALT, total bilirubin, albumin, total protein, and ALP were measured as markers of hepatocellular and biliary injury. Blood urea nitrogen and creatinine were detected as renal function indexes. The measurements were performed by the Comparative Pathology Laboratory of the Massachusetts Institute of Technology Division of Comparative Medicine.

Innate Immune Response. To evaluate potential innate immune responses to systemically delivered pacDNAs, immunocompetent C57BL/6 mice (n = 4) were injected i.v. with samples and controls at an equal ASO concentration (0.5 µmol/kg; free polymer concentration equals that of the pacDNA). LPS (15 μ g per animal) was used as a positive control. Two hours postinjection, serum samples were collected and processed to measure the representative cytokines (IL-1α, IL-1β, IL-4, IL-6, IL-10, IL-12 [p70], IFN- γ , and TNF- α) using ELISA kits according to the manufacturer's protocol (Bio-Plex Mouse Cytokine Group I 8-plex Assay-Z6000004JP; Bio-Rad Laboratories, Inc.).

Adaptive Anti-PEG Immunity and Accelerated Blood Clearance. Healthy C57BL/6 mice (6 to 8 wk, n = 4) were administered Cy5-labeled PO pacDNA, PS pacDNA, and free bottlebrush polymer via the tail vein on days 1, 4, 11, and 25 at a dosage of 0.5 µmol/kg (ASO-basis; free polymer concentration equals that of the pacDNAs). Blood samples (25 µL) were collected from the submandibular vein at preselected postinjection time points (0 min, 30 min, and 4, 8, and 24 h). The concentration of circulating anti-PEG IgM and IgG antibodies was assessed by ELISA (Mouse Anti-PEG IgM ELISA and Mouse Anti-PEG IgG ELISA; Life Diagnostics Inc.), according to the manufacturer's protocol. PK parameters were calculated using the similar method mentioned above.

To study the generation of anti-PEG immunoglobins following frequent exposures to pacDNA or conventional linear PEG-ASO conjugate in the blood, male C57BL/6 mice in groups of five were i.v. injected with pacDNAs (PO and PS), bottlebrush polymer, or yPEG-PS ASO at a dosage of 0.5 µmol/kg once every 3 d for 36 d (12 injections total). The serum of mice was collected on the seventh and the 14th day after the last injection, and the concentrations of circulating anti-PEG IgM and IgG antibodies were assessed by ELISA.

Statistics. All in vitro experiments were repeated at least three times. Statistical analysis was performed using GraphPad Prism 9. Data are presented as mean \pm SD. Statistical methods used are indicated in the figure legends. Statistical significance was set at *P < 0.05, **P < 0.01, ***P < 0.001, or ****P < 0.0001.

Data Availability. All study data are included in the article and/or SI Appendix.

- M. B. Ryan, R. B. Corcoran, Therapeutic strategies to target RAS-mutant cancers. Nat. Rev. Clin. Oncol. 15, 709-720 (2018).
- D. K. Simanshu, D. V. Nissley, F. McCormick, RAS proteins and their regulators in human disease. Cell 170, 17-33 (2017).
- A. R. Moore, S. C. Rosenberg, F. McCormick, S. Malek, RAS-targeted therapies: Is the undruggable drugged? Nat. Rev. Drug Discov. 19, 533-552 (2020).
- L. Chin et al., Essential role for oncogenic Ras in tumour maintenance. Nature 400, 468-472
- H. Ying et al., Oncogenic Kras maintains pancreatic tumors through regulation of anabolic glucose metabolism. Cell 149, 656-670 (2012).
- G. H. Fisher et al., Induction and apoptotic regression of lung adenocarcinomas by regulation of a K-Ras transgene in the presence and absence of tumor suppressor genes. Genes Dev. 15, 3249-3262 (2001).
- J. M. Ostrem, U. Peters, M. L. Sos, J. A. Wells, K. M. Shokat, K-Ras(G12C) inhibitors allosterically control GTP affinity and effector interactions. Nature 503, 548-551 (2013).
- R. Rosell, A. Aguilar, C. Pedraz, I. Chaib, KRAS inhibitors, approved. Nat. Can. 2, 1254-1256 (2021).
- A. D. Cox, S. W. Fesik, A. C. Kimmelman, J. Luo, C. J. Der, Drugging the undruggable RAS: Mission possible? Nat. Rev. Drug Discov. 13, 828-851 (2014).
- S. T. Crooke, B. F. Baker, R. M. Crooke, X. H. Liang, Antisense technology: An overview and prospectus. Nat. Rev. Drug Discov. 20, 427-453 (2021).
- S. J. Ross et al., Targeting KRAS-dependent tumors with AZD4785, a high-affinity therapeutic antisense oligonucleotide inhibitor of KRAS. Sci. Transl. Med. 9, eaal5253 (2017).
- S. Kamerkar et al., Exosomes facilitate therapeutic targeting of oncogenic KRAS in pancreatic cancer. Nature 546, 498-503 (2017).
- S. Bajan, G. Hutvagner, RNA-based therapeutics: From antisense oligonucleotides to miRNAs. Cells 9, 137 (2020).
- 14. S. M. Hammond et al., Delivery of oligonucleotide-based therapeutics: Challenges and opportunities. EMBO Mol. Med. 13, e13243 (2021).
- T. C. Roberts, R. Langer, M. J. A. Wood, Advances in oligonucleotide drug delivery. Nat. Rev. Drug Discov. 19, 673-694 (2020).
- K. Sridharan, N. J. Gogtay, Therapeutic nucleic acids: Current clinical status. Br. J. Clin. Pharmacol. 16. 82. 659-672 (2016).
- V. K. Sharma, J. K. Watts, Oligonucleotide therapeutics: Chemistry, delivery and clinical progress. Future Med. Chem. 7, 2221–2242 (2015).
- R. L. Juliano, The delivery of therapeutic oligonucleotides. Nucleic Acids Res. 44, 6518-6548 (2016).
- 19. U. Lächelt, E. Wagner, Nucleic acid therapeutics using polyplexes: A journey of 50 years (and beyond). Chem. Rev. 115, 11043-11078 (2015).
- 20. D. Luo, W. M. Saltzman, Synthetic DNA delivery systems. Nat. Biotechnol. 18, 33-37 (2000).
- A. A. Levin, S. P. Henry, Toxicology of oligonucleotide therapeutics and understanding the relevance of the toxicities. Pharmaceutical Sciences Encyclopedia: Drug Discovery, Development, and Manufacturing 24, 1-38 (2010).
- T. Yamamoto, M. Nakatani, K. Narukawa, S. Obika, Antisense drug discovery and development. Future Med. Chem. 3, 339-365 (2011).
- R. Juliano, M. R. Alam, V. Dixit, H. Kang, Mechanisms and strategies for effective delivery of antisense and siRNA oligonucleotides. Nucleic Acids Res. 36, 4158-4171 (2008).
- A. Khvorova, J. K. Watts, The chemical evolution of oligonucleotide therapies of clinical utility Nat. Biotechnol. 35, 238-248 (2017).
- W. B. Wan, P. P. Seth, The medicinal chemistry of therapeutic oligonucleotides. J. Med. Chem. 59, 9645-9667 (2016).
- F. Eckstein, Phosphorothioates, essential components of therapeutic oligonucleotides. Nucleic Acid Ther. 24, 374-387 (2014).
- 27. E. Koller et al., Mechanisms of single-stranded phosphorothioate modified antisense oligonucleotide accumulation in hepatocytes. Nucleic Acids Res. 39, 4795-4807 (2011).
- R. S. Geary, D. Norris, R. Yu, C. F. Bennett, Pharmacokinetics, biodistribution and cell uptake of antisense oligonucleotides. Adv. Drug Deliv. Rev. 87, 46-51 (2015).
- M. J. Graham et al., In vivo distribution and metabolism of a phosphorothioate oligonucleotide within rat liver after intravenous administration. J. Pharmacol. Exp. Ther. 286, 447-458 (1998).
- S. P. Henry, H. Bolte, C. Auletta, D. J. Kornbrust, Evaluation of the toxicity of ISIS 2302, a phosphorothioate oligonucleotide, in a four-week study in cynomolgus monkeys. Toxicology 120,
- S. P. Henry, W. Novotny, J. Leeds, C. Auletta, D. J. Kornbrust, Inhibition of coagulation by a phosphorothioate oligonucleotide. Antisense Nucleic Acid Drug Dev. 7, 503-510 (1997).

ACKNOWLEDGMENTS. Research reported in this publication was supported by the National Cancer Institute (Grant Number R01CA251730), the National Institute of General Medical Sciences (Grant Number R01GM121612), and the NSF (DMR Grant Number 2004947). The content is solely the responsibility of the authors and does not necessarily represent the official views of the NIH or the NSF. We thank the Institute for Chemical Imaging of Living System at Northeastern University for consultation and imaging support. We also thank the Koch Institute Swanson Biotechnology Center for support with microscopy and histology, which is funded in part by the Cancer Center Support (Grant Number P30CA14051) from the National Cancer Institute. We thank Northeastern University Research Computing for providing the highperformance computing resource (the Discovery cluster).

- 32. K. Hovingh, J. Besseling, J. Kastelein, Efficacy and safety of mipomersen sodium (Kynamro). Expert Opin. Drug Saf. 12, 569-579 (2013).
- X. Lu et al., Providing oligonucleotides with steric selectivity by brush-polymer-assisted compaction. J. Am. Chem. Soc. 137, 12466-12469 (2015).
- F. Jia et al., Depth-profiling the nuclease stability and the gene silencing efficacy of brusharchitectured poly (ethylene glycol)-DNA conjugates. J. Am. Chem. Soc. 139, 10605-10608
- 35. F. Jia et al., Effect of PEG architecture on the hybridization thermodynamics and protein accessibility of PEGylated oligonucleotides. Angew. Chem. Int. Ed. Engl. 56, 1239-1243 (2017).
- D. Wang et al., Bottlebrush-architectured poly(ethylene glycol) as an efficient vector for RNA interference in vivo. Sci. Adv. 5, eaav9322 (2019).
- 37. J. M. Harris, R. B. Chess, Effect of pegylation on pharmaceuticals. Nat. Rev. Drug Discov. 2, 214-221 (2003)
- AstraZeneca Clinical Trials, Phase 1 dose-escalation study of AZD4785 in patients with advanced solid tumors. https://astrazenecagrouptrials.pharmacm.com/ST/Submission/View?id=24623. Accessed 1 September 2019.
- M. Herkt, T. Thum, Pharmacokinetics and proceedings in clinical application of nucleic acid therapeutics. Mol. Ther. 29, 521-539 (2021).
- E. W. Ng et al., Pegaptanib, a targeted anti-VEGF aptamer for ocular vascular disease. Nat. Rev. Drug Discov. 5, 123-132 (2006).
- 41. R. K. O'Reilly, M. J. Joralemon, K. L. Wooley, C. J. Hawker, Functionalization of micelles and shell cross-linked nanoparticles using click chemistry. Chem. Mater. 17, 5976-5988 (2005).
- 42. A. Balijepalli, J. W. Robertson, J. E. Reiner, J. J. Kasianowicz, R. W. Pastor, Theory of polymernanopore interactions refined using molecular dynamics simulations. J. Am. Chem. Soc. 135, 7064-7072 (2013).
- 43. S. T. Crooke, S. Wang, T. A. Vickers, W. Shen, X. H. Liang, Cellular uptake and trafficking of antisense oligonucleotides. Nat. Biotechnol. 35, 230-237 (2017).
- 44. L. A. Yakubov et al., Mechanism of oligonucleotide uptake by cells: Involvement of specific receptors? Proc. Natl. Acad. Sci. U.S.A. 86, 6454-6458 (1989).
- C. H. J. Choi, L. Hao, S. P. Narayan, E. Auyeung, C. A. Mirkin, Mechanism for the endocytosis of spherical nucleic acid nanoparticle conjugates. Proc. Natl. Acad. Sci. U.S.A. 110, 7625-7630
- 46. H. Ding et al., DNA nanostructure-programmed like-charge attraction at the cell-membrane interface. ACS Cent. Sci. 4, 1344-1351 (2018).
- 47. E. Linnane et al., Differential uptake, kinetics and mechanisms of intracellular trafficking of nextgeneration antisense oligonucleotides across human cancer cell lines. Nucleic Acids Res. 47, 4375-4392 (2019).
- 48. G. T. Kozma, T. Shimizu, T. Ishida, J. Szebeni, Anti-PEG antibodies: Properties, formation, testing and role in adverse immune reactions to PEGylated nano-biopharmaceuticals. Adv. Drug Deliv. Rev. 154-155, 163-175 (2020).
- 49. P. Shieh, H. V. T. Nguyen, J. A. Johnson, Tailored silyl ether monomers enable backbonedegradable polynorbornene-based linear, bottlebrush and star copolymers through ROMP. Nat. Chem. 11, 1124-1132 (2019).
- 50. H. Li et al., Well-defined DNA-polymer miktoarm stars for enzyme-resistant nanoflares and carrier-free gene regulation. Bioconjug. Chem. 31, 530-536 (2020).
- 51. F. Jia et al., Improving the enzymatic stability and the pharmacokinetics of oligonucleotides via DNA-backboned bottlebrush polymers. Nano Lett. 18, 7378-7382 (2018).
- Y. Wang et al., Self-assembled DNA-PEG bottlebrushes enhance antisense activity and pharmacokinetics of oligonucleotides. ACS Appl. Mater. Interfaces 12, 45830-45837 (2020).
- 53. D. Wang et al., Precision tuning of DNA-and poly (ethylene glycol)-based nanoparticles via coassembly for effective antisense gene regulation. *Chem. Mater.* **29**, 9882–9886 (2017).

 J. A. Love, J. P. Morgan, T. M. Trnka, R. H. Grubbs, A practical and highly active ruthenium-based
- catalyst that effects the cross metathesis of acrylonitrile. Angew. Chem. Int. Ed. 41, 4035-4037 (2002)
- S. J. Marrink, H. J. Risselada, S. Yefimov, D. P. Tieleman, A. H. de Vries, The MARTINI force field: Coarse grained model for biomolecular simulations. J. Phys. Chem. B 111, 7812-7824
- H. Lee, A. H. de Vries, S.-J. Marrink, R. W. Pastor, A coarse-grained model for polyethylene oxide and polyethylene glycol: Conformation and hydrodynamics. J. Phys. Chem. B 113, 13186-13194
- H. J. Berendsen, J. v. Postma, W. F. van Gunsteren, A. DiNola, J. R. Haak, Molecular dynamics with coupling to an external bath. J. Chem. Phys. 81, 3684-3690 (1984).
- D. Van Der Spoel et al., GROMACS: Fast, flexible, and free. J. Comput. Chem. 26, 1701-1718